Int. J. Electrochem. Sci., 17 **(2022)** Article Number: 220137, doi: 10.20964/2022.02.06

International Journal of
ELECTROCHEMICAL
SCIENCE
www.electrochemsci.org

Corrosion behavior of Al-Ce alloys in 3.5%NaCl solution

Xianjie Zhou[1], *Hanqing Xiong*[1,2,*]

[1] Shenzhen APG Material Technology Co.Ltd (APG), Shenzhen 518000, China
[2] Department of Mechanical and Electronic Engineering, Changsha University, Changsha 410022, China
[*]E-mail: xhanqing@163.com

Received: 15 September 2021 / *Accepted:* 19 October 2021 / *Published:* 6 December 2021

The corrosion behavior of Al-xCe alloys was researched by microstructure characterization analysis, electrochemical and immersion tests in 3.5% NaCl solution. The result shows that the volume fraction of Al_4Ce phases increases notably with the increasing content Ce element, and Al_4Ce phase is the main part of Al-50wt%Ce alloy matrix. The corrosion mechanism is attributed to the potential difference between Al_4Ce and α-Al phases causing the galvanic corrosion. Al-15wt%Ce, Al-30wt%Ce and Al-50wt%Ce alloys exhibit different corroded characteristics. For Al-15wt%Ce and Al-30wt%Ce alloys, Al_4Ce phase is dissolved due to the anode effect. For Al-50wt%Ce alloy, α-Al phase are peeling off without enough support during the corrosion process. The corrosion rate of Al-xCe alloys increases in following order: Al-15wt%Ce > Al-50wt%Ce > Al-30wt%Ce. Thus, the corrosion behavior of Al-xCe alloys is related to the volume fraction of Al_4Ce phases.

Keywords: Al-Ce alloy; Microstructure; Corrosion behavior; Alloy target material

1. INTRODUCTION

With high specific strength, superior fracture toughness and good anti-corrosion property, Al alloys are extensively attractive structural materials in aerospace, military, shipping and transportation industries [1]. In addition, Al element exhibits excellent coating properties, such as high resolution, low electrical resistivity and high resistance to hillock formation, suitable for optical, microelectronics, telecommunications [2]. Thus, Al and its alloys also can be used as target materials for preparing thin films to improve optical, thermal, electrical and chemical properties [3, 4]. Through optimizing various parameters and methods, many physical and chemical methods have been developed for specific coating applications [5, 6]. These techniques include sputtering, vacuum, magnetic fields, gas chemistry and thermal evaporation [7]. The main drawback of Al alloy target materials is the use of toxic elements,

which result in environmental pollution and human health [8, 9]. Thus, the alloying element selections are important for Al alloy target materials. Due to excellent optical, electromagnetic and other physical properties, rare earth (RE) elements can be combined with Al to form a variety of new alloy target materials with different properties [10]. Ce element is relatively inexpensive as an alloying element, which is the most abundant of the rare earth metals and a by-product of rare earth mining efforts [11]. Al-Ce alloy system has an excellent high-temperature mechanical performance among Al alloys [12]. Sims et al [13] prepared Al-Ce alloy through powder metallurgy and mechanical alloying techniques, and the result revealed the high thermal stability of Al alloy containing high Ce content. Al-Ce coatings deposited by magnetron sputtering were reported for corrosion protection of AA6061 [14]. The Al-Ce films can also offer additional anti-corrosion functionality to AA2024 alloy due to active corrosion protection [15]. The recent report indicated that Al-Ce alloy films have comprehensive application foreground and spread value in the automotive industry [16]. However, the excellent Al-Ce films require appropriate Al-Ce alloy target materials. The aim of the present study is to investigate the microstructure and corrosion behavior of Al-Ce alloy target materials with different Ce contents, Al-15wt%Ce, Al-30wt%Ce and Al-50wt%Ce alloys.

2. MATERIALS AND EXPERIMENTAL PROCEDURES

The Al-xCe(x=15%, 30% and 50%, wt%) alloys were fabricated by melting pure Al (99.999%) and Ce (99.9%) using a medium-frequency induction furnace under the vacuum condition. The casting ingots were achieved by the conventional casting method using a copper mold. X-ray diffraction (XRD, DMAX-2500X) were used to identify alloy phases of Al-xCe alloys. Scanning electron microscope (SEM, JEOL, JSM-6510A) equipped with energy-dispersive spectrometry (EDS) were conducted to analyze microstructure of experimental alloys. Before SEM observation, the alloy samples were ground with abrasive paper from 200 to 2000 grit, and then the samples were polished with diamond paste. During SEM observation, backscattered electron imaging (BSE) were adopted, and the component analysis of alloy phases was also carried out.

The three-electrode system comprised of the reference electrode (Ag/AgCl), the counter electrode (platinum plate) and the working electrode (experimental samples) was employed to measure electrochemical performance of experimental alloys. During electrochemical testing, it used 3.5% NaCl solution as the electrolyte and Adminal electrochemical workstation (Squidstat Plus, USA) as the recording equipment. The open circuit potential (OCP) was obtained after alloy samples were immersed for 30 min. Potentiodynamic polarization curve was obtained from -300 to +300 mV (vs. Ag/AgCl) with respect to OCP, and the scanning rate was 1 $mV \cdot s^{-1}$. Electrochemical impedance spectroscopy (EIS) was tested with respect to OCP, the frequency range was from 100 kHz to 0.01Hz and the voltage amplitude was 5 mV.

In order to evaluate corrosion rate of experimental alloys, the alloy samples were immersed in 3.5% NaCl solution for 168 h. Before the test, the initial weight of alloy samples were obtained after cleaning and drying. After the test, the tested samples were cleaned with 2% CrO_3 and 5% H_3PO_4 distilled water to remove corrosion products and dried, then the weight loss of immersion test was

obtained. The corrosion morphology of immersed samples was further observed and analyzed using SEM.

3. RESULTS AND DISCUSSION

3.1 Microstructure

Figure 1 displays XRD patterns of Al-15wt%Ce, Al-30wt%Ce and Al-50wt%Ce alloys. For Al-15wt%Ce alloy, α-Al and Al_4Ce phases are identified by the XRD pattern in Figure 1a. Al_4Ce phase is created from the eutectic reaction ($L \rightarrow$ α-Al + Al_4Ce) due to the different electronegativity values of Al (1.61) and Ce (1.12) elements. With the content of Ce element increasing, Al-30wt%Ce alloy is also comprised of α-Al and Al_4Ce phases, as shown in Figure 1b. In addition to α-Al and Al_4Ce phases, $Al_{11}Ce_3$ phase is detected in Al-50wt%Ce alloy from Figure 1c in spite of very low content. Figure 2 shows the BSE images and corresponding EDS patterns of Al-xCe alloys. As shown in Figure 2a1, Al-15wt%Ce alloy presents the obvious as-cast structure including black matrix, coarse white dendrites and fine white lamellar precipitates. The EDS patterns based on Figure a2 and a3 indicate that the black matrix is α-Al, while both dendrites and fine lamellar precipitates are Al_4Ce phases. In Al-30wt%Ce alloy, black matrix, coarse dendrites and fine lamellar precipitates can also be observed in Figure b1. Furthermore, the similar phase component is confirmed according to the EDS patterns (Figure b2 and b3). With the further increase of Ce content, the microstructure characteristics of Al-50wt%Ce alloy is different from Al-15wt%Ce and Al-30wt%Ce alloys. It can be seen from Figure 2c1 that coarse white dendrites cover the whole alloy matrix, and the dendrites is proved to be Al_4Ce phase with EDS analysis (Figure 2c2). Small amount of α-Al phases distribute along the dendrites, and moreover granular $Al_{11}Ce_3$ phases could exist between Al_4Ce and α-Al phase, which are also identified by the XRD and EDS analysis (Figure 1c and Figure 2c3). The formation of $Al_{11}Ce_3$ phase could attribute to the non-equilibrium freezing during the conventional casting process. Thus, Powell [17] indicated that $Al_{11}RE_3$ phase was similar with Al_4RE phases in the previous literature.

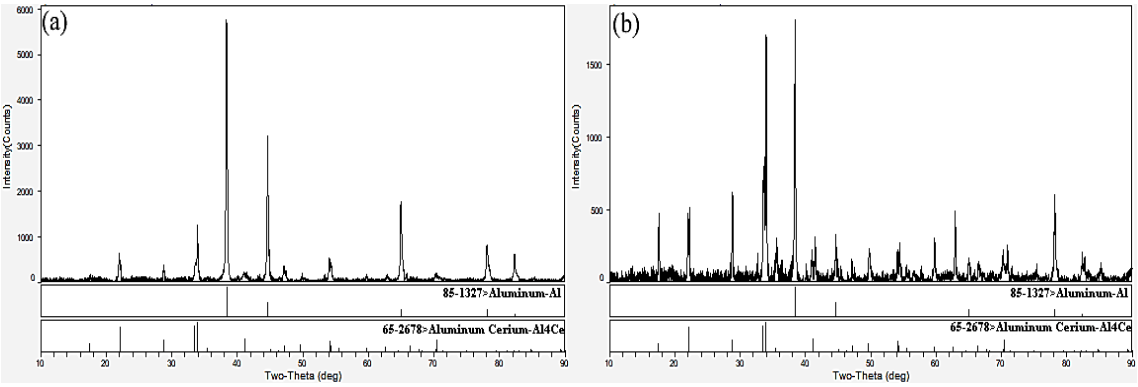

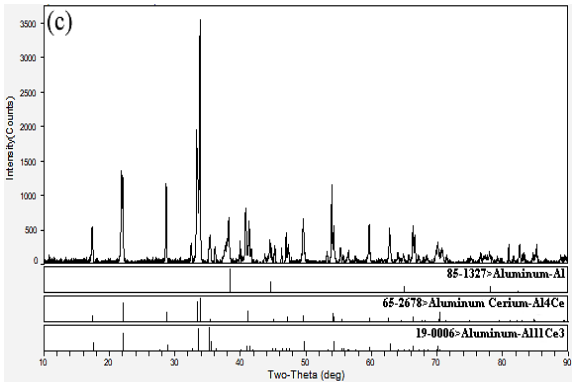

Figure 1. XRD patterns of Al-15wt%Ce (a), Al-30wt%Ce (b) and Al-50wt%Ce (c) alloys

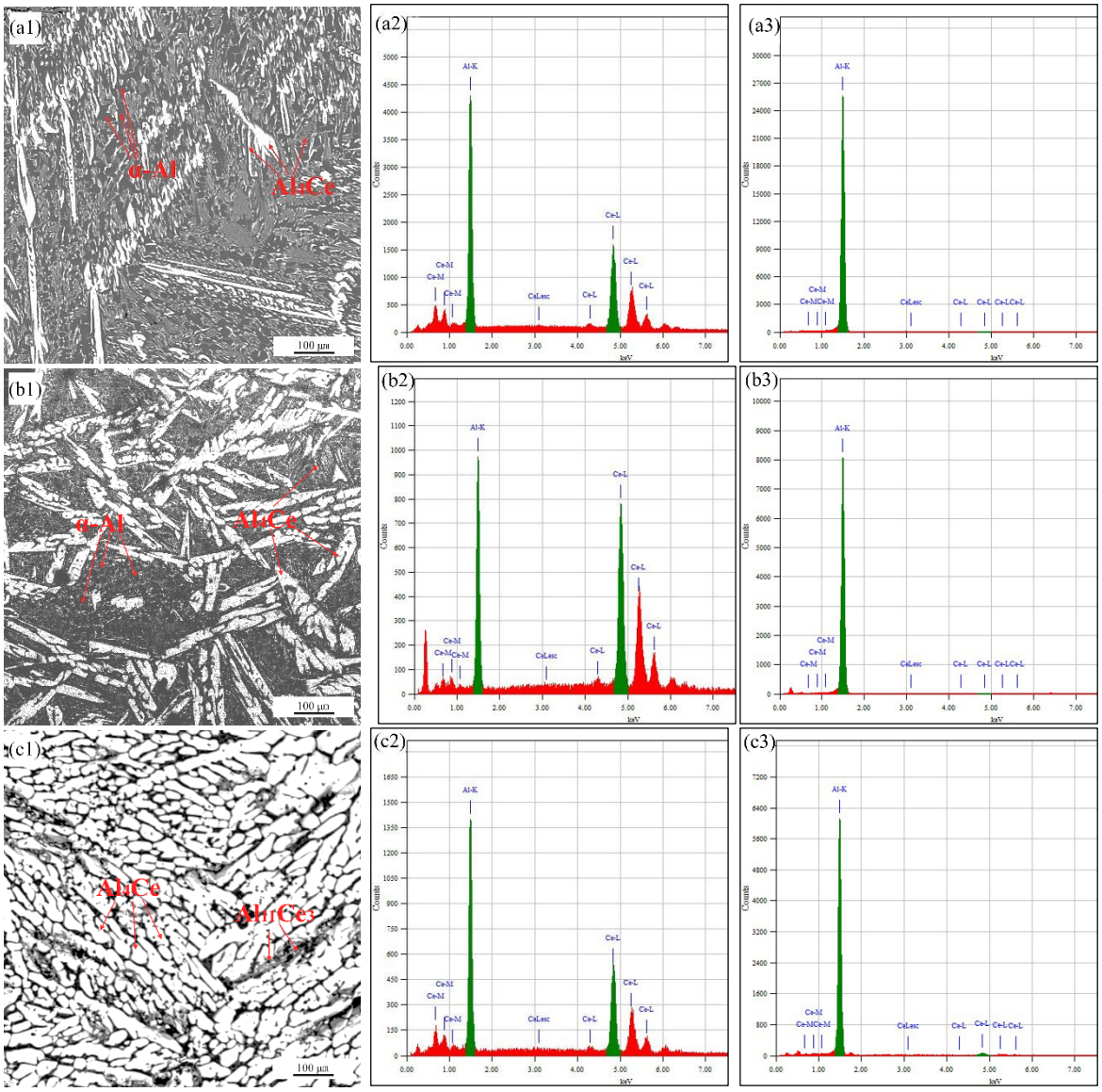

Figure 2. BSE images and EDS patterns of experimental alloys, (a1) Al-15wt%Ce, (a2) Al_4Ce phase, (a3) α-Al, (b1) Al-30wt%Ce, (b2) Al_4Ce phase, (b3) α-Al, (c1) Al-50wt%Ce, (c2) Al_4Ce phase and (c3) α-Al.

3.2 Electrochemical measurement

Figure 3 shows open circuit potential (OCP) and potentiodynamic polarization curves of Al-15wt%Ce, Al-30wt%Ce and Al-50wt%Ce alloys in 3.5%NaCl solution, and corresponding corrosion parameters are listed in Table 1. The OCP value is the potential difference between the working electrode and the reference electrode without the external load. The OCP curve can indicate the electrochemical activity of Al alloys, since the dynamic relationship of corrosion process can be reflected by the initial OCP [18]. In Figure 3a, the relatively stable OCP values are obtained through the curves after a small decline. Furthermore, it can be seen that the OCP values of Al-xCe alloys in the following order: Al-15wt%Ce < Al-30wt%Ce < Al-50wt%Ce. In Figure 3b, the Al-xCe alloys show similar polarization curves, but the corrosion potentials (E_{corr}) of Al-xCe alloys exhibit a downtrend, indicating that the corrosion driving force of Al-xCe alloys is increased with the increasing Ce content. This variation trend is in keeping with the result of OCP test. The corrosion current densities (J_{corr}) of experimental alloys are evaluated by Tafel extrapolation, and the result shows that the J_{corr} value of Al-xCe alloys firstly increases and then decreases with the increase of Ce content. According to XRD patterns, Al-15wt%Ce and Al-30wt%Ce alloys all contain Al_4Ce and α-Al phases. In addition to the two phases, a few of $Al_{11}Ce_3$ phase exists in Al-50wt%Ce alloy. Since $Al_{11}Ce_3$ phase is similar with Al_4Ce phase [17], the change of electrochemical property can be analyzed through Al_4Ce phase. Usually, α-Al matrix shows the corrosion potential of -0.75 V vs SCE (saturated calomel electrode) in NaCl solution [19], and the electrode potential of Ce is -2.48 V [20]. The OCP value of Al-xCe alloys is decreased after the addition of Ce element, the E_{corr} values present a same downtrend. Although the electrode potential of Al_4Ce phase is not determined exactly, the electrochemical potential of Ce is similar to that of Mg (-2.37 V). A little Ce element can reduce the corrosion rate of Al alloys, but an excessive Ce addition can result in the increase of corrosion rate [21]. In the report by Huang [22], the electrode potential of $Al_{12}Mg_{17}$ phase is -1.028 V, which is lower than α-Al matrix. It can be expected that Al_4Ce phase is weak anode phase in the Al-xCe alloys. Thus, the galvanic corrosion is formed between Al_4Ce phase and α-Al matrix, the Al_4Ce phase is preferentially corroded. The size of Al_4Ce phase is distinctly coarsening for Al-30wt%Ce alloy, as shown in Figure 2. When the content of Ce element is increased from 15wt% to 30wt%, the J_{corr} value is in a strong uptrend because of enough galvanic couples. However, the matrix of Al-50wt%Ce alloy is covered in Al_4Ce phases, the number of α-Al cathode phases is dropped dramatically in view of XRD patterns and EDS analysis. Although the lower E_{corr} and higher driving force of Al-50wt%Ce alloy, the corrosion process is limited due to less cathode phases which can merely form a small number of galvanic couples. Thus, Al-50wt%Ce alloy exhibits lower J_{corr} than that of Al-30wt%Ce one.

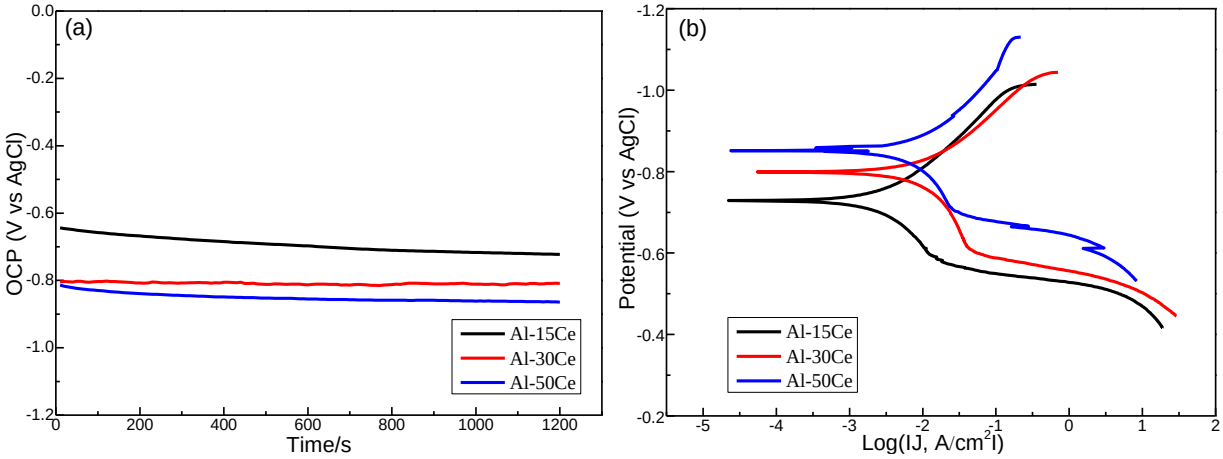

Figure 3. Open circuit potential (a) and Potentiodynamic polarization curve (b) of Al-15wt%Ce, Al-30wt%Ce and Al-50wt%Ce alloys in 3.5%NaCl solution.

Table 1. Corrosion parameters of Al-15wt%Ce (a), Al-30wt%Ce (b) and Al-50wt%Ce (c) alloys in 3.5% NaCl solution.

Solution-treated alloys	OCP/V(vs AgCl)	E_{corr}/V(vs AgCl)	j_{corr}/(A·cm^{-2})
Al-15wt%Ce	-0.722	-0.728	0.447×10^{-3}
Al-30wt%Ce	-0.809	-0.798	1.383×10^{-3}
Al-50wt%Ce	-0.904	-0.851	0.613×10^{-3}

Figure 4 displays Nyquist and Bode plots of three experimental alloys. In Figure 4a, the three Al-xCe alloys present similar Nyquist curves comprised of a capacitive loop at the high-frequency region and an inductive capacitive loop at the low-frequency region. The capacitive loop represents an electric double layer in which the charge transfer exists between experimental alloys and test electrolyte [23]. Although Al alloys possess a layer of compact oxide film, the inductive loop is related to the breakdown of oxide film due to the galvanic effect from noble potential impurities and active precipitates [24, 25]. Obviously, the potential difference between Al_4Ce phase and α-Al matrix accelerate the surface pitting. Thus, this initial process is simulated by the equivalent circuit as shown in Fig. 4c and the fitting values of impedance parameters are listed in Table 2. It should be noted that constant phase element (CPE) is substituted for the double-layer capacitance element (C) and is expressed by Equation (1) [26]:

$$z(j\omega) = (Y_0)^{-1}(j\omega)^{-n} \qquad (1)$$

It should be noted that Y_0 represents the CPE-constant, j is imaginary unit, n is CPE-power ($0 \leq n \leq 1$) and ω is angular frequency ($\omega = 2\pi f$, f is the frequency). CPE indicates the pure capacitance when n reaches 1, while the n value between 0 and 1 reflects heterogeneous effects. Accordingly, R_S is the solution resistance in the equivalent circuit, CPE_1 corresponds to the double-layer capacitance between experimental sample and electrolyte, R_t is the charge transfer resistance, and moreover R_L accompanied by L denote the destroying of oxide film due to the initial pitting of experimental alloys. Furthermore, it can be seen that the simulated equivalent circuit is very close to the electrochemical process of alloy

surface due to the small χ^2 values. Table 2 shows that R_t value of Al-xCe alloys firstly decreases and then increases with the increase of Ce content. Figure 4b gives bode plots of Al-xCe alloys, which presents the relationship between impedance modulus (|Z|) and frequency. Obviously, |Z| value of Al-xCe alloys displays a similar variation tendency with R_t value. |Z| and R_t values also reflect the corrosion rate of Al-xCe alloys since the exchange current is directly connected to the electrochemical corrosion. Thus, the result of EIS test is consistent with polarization measurements.

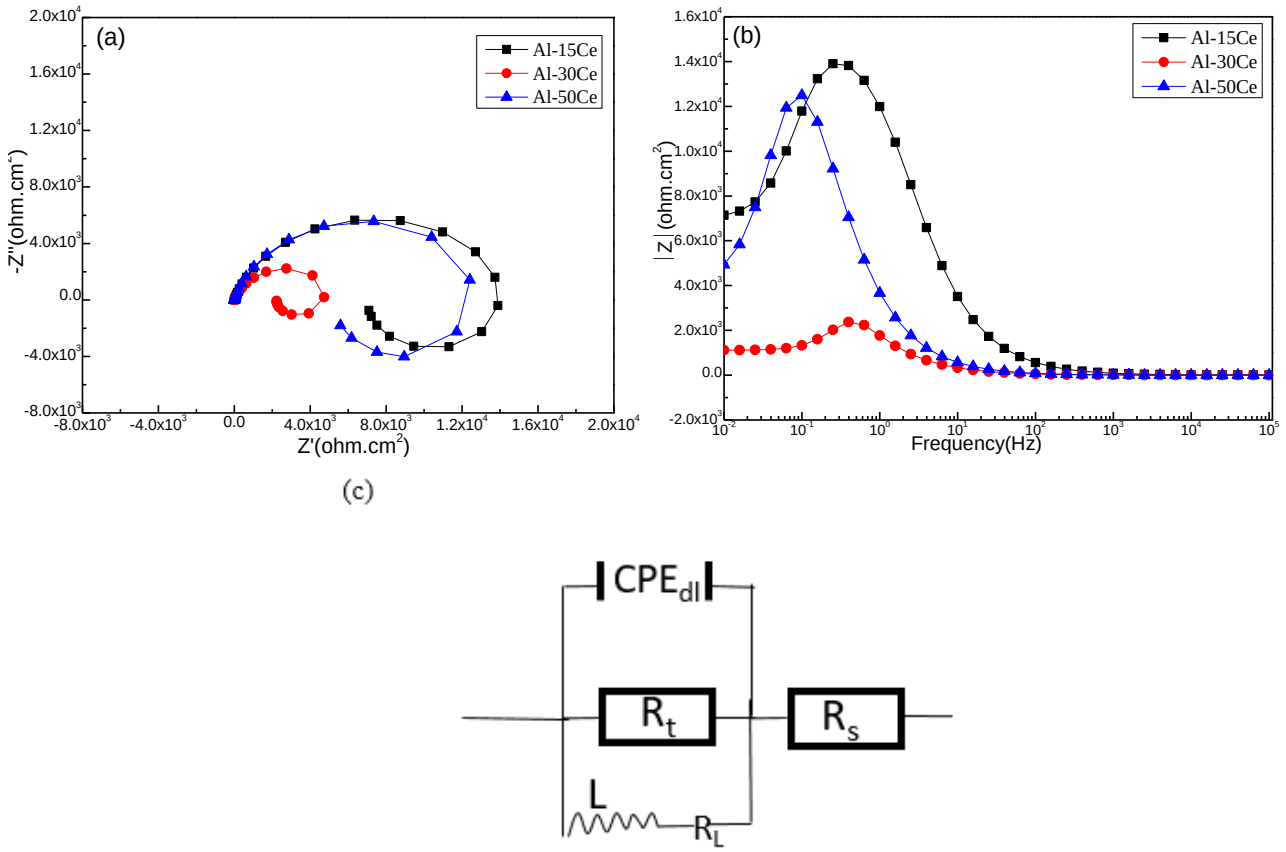

Figure 4. Impedance spectrum of Al-15wt%Ce, Al-30wt%Ce and Al-50wt%Ce alloys in 3.5%NaCl solution. (a) Nyquist plot, (b) Bode plot and (c) Equivalent circuit used for fitting EIS data.

Table 2. EIS simulated data of Al-15wt%Ce, Al-30wt%Ce and Al-50wt%Ce alloys in 3.5%NaCl solution.

Al-xCe alloys	Al-15wt%Ce	Al-30wt%Ce	Al-50wt%Ce
Rs ($\Omega \cdot cm^2$)	3.386	4.95	3.686
CPE_1 ($\Omega^{-1} \cdot cm^{-2} \cdot s^n$)	5.327×10^{-5}	5.359×10^{-5}	8.355×10^{-6}
n_1 ($0 < n < 1$)	0.8437	0.8003	0.8309
R_t ($\Omega \cdot cm^2$)	14950	7077	15120
L_1($H \cdot cm^2$)	6.04×10^{-4}	1.808×10^{-5}	4.436×10^{-4}
R_L	5787	3251	7556
χ^2	2.083×10^{-3}	9.346×10^{-3}	1.274×10^{-3}

3.3 Immersion Test

Figure 5 compares the corrosion rates of Al-15wt%Ce, Al-30wt%Ce and Al-50wt%Ce alloys after immersion test. It can be seen that the corrosion rate firstly presents an upward trend and then a downward trend. The Al-15wt%Ce alloy shows the lowest corrosion rate, while the Al-30wt%Ce alloy show the highest rate. This immersion result accords basically with polarization and EIS measurements.

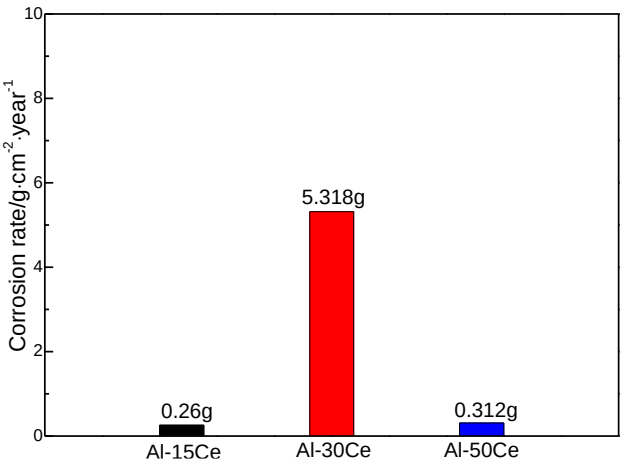

Figure 5. Corrosion rate of Al-15wt%Ce, Al-30wt%Ce and Al-50wt%Ce alloys evaluated after immersed in 3.5%NaCl solution for 168h.

In order to analyze the corrosion mechanism of Al-xCe alloys, the corrosion products on the surface of experimental alloys are removed, and the corrosion morphologies are shown in Figure 6. It can be observed that different corroded features are on the surfaces of Al-15wt%Ce, Al-30wt%Ce and Al-50wt%Ce alloys, respectively. In Figure 6a, a mixed characteristics comprised of pits and few local corrosion on the surface of Al-15wt%Ce alloy. Furthermore, the depth of corroded pits is so shallow and the local corrosion also includes shallow pits. This phenomenon indicates a weak corrosion process for Al-15wt%Ce alloy. Li et al [27] reported that Ce element was beneficial to enhancing the stability of the surface film and improving the corrosion resistance of Al-Mg-Mn alloy. It can also be introduced into the Al coating as a potential corrosion inhibitor slowing down the corrosion process [15]. However, Zhang et al [28] found that the pitting corrosion sensibility of Al alloys was increased because the addition of Ce element promoted the ion diffusion through the passive film. Actually, Al_4Ce phase has lower corrosion potential than that of α-Al matrix leading to a formation of pitting. When excessive Ce element is added, the anode effect is increased and the protective effect of passive film is reduced. With the increase of Ce addition, Al-30wt%Ce alloy evidently exhibit a poor anti-corrosion, as shown in Figure 6b. Compared with Al-15wt%Ce alloy, more serious local corrosion occurs on the surface of Al-30wt%Ce alloy. Furthermore, coarse corrosion cracks and corroded matrix are also observed, which indicates that the alloy matrix is easily destroyed. In Figure 6c, lot of hairline corrosion cracks are filled with the surface of Al-50wt%Ce alloy. According to EDS and XRD analysis, Al_4Ce phase is the main

part of Al-50wt%Ce alloy matrix, while only a few α-Al phases distribute at the edge of Al_4Ce phases. For Al-50wt%Ce alloy, the resistance of electrochemical corrosion process is increased on account of the reducing cathode effect. During the galvanic corrosion process, α-Al phase as cathode are peeling off without enough support. Therefore, the immersion test also shows that the corrosion resistance increases in the order: Al-15wt%Ce > Al-50wt%Ce > Al-30wt%Ce.

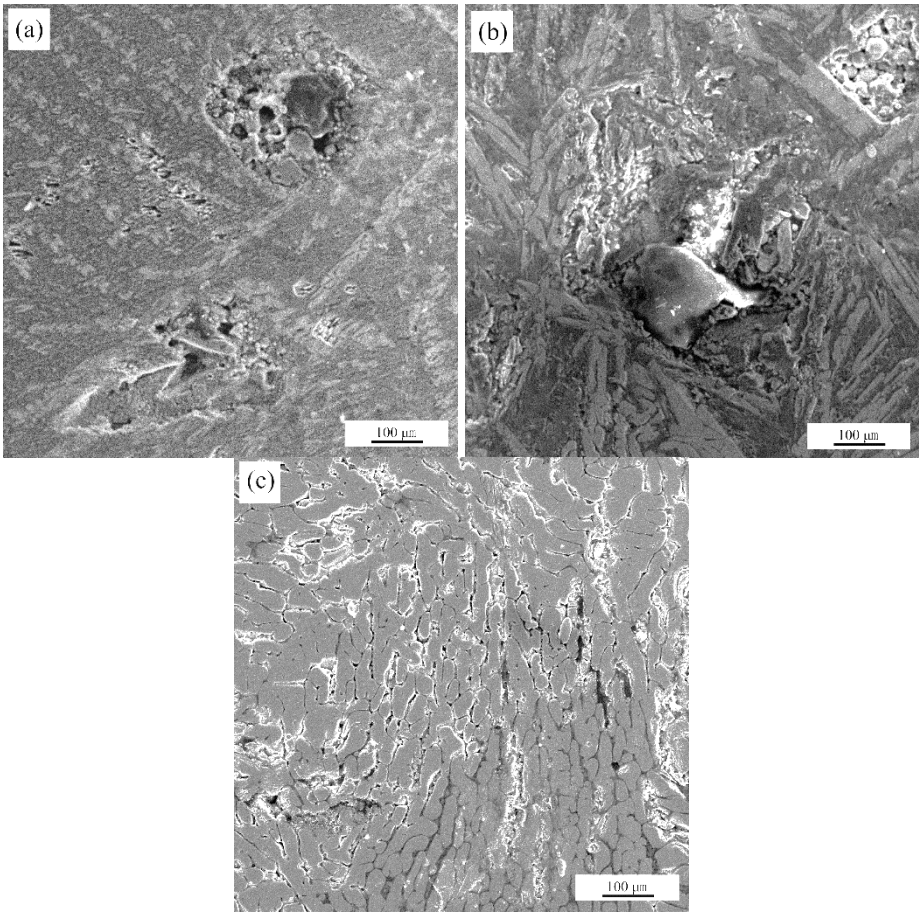

Figure 6. Corrosion morphologies of Al-15wt%Ce, Al-30wt%Ce and Al-50wt%Ce alloys in 3.5%NaCl solution immersed for 168h.

4. CONCLUSIONS

1) With the increasing content Ce element, the volume fraction of Al_4Ce phases increases notably in Al-xCe alloy matrix, Al_4Ce phase is the main part of Al-50wt%Ce alloy matrix.

2) Al-15wt%Ce, Al-30wt%Ce and Al-50wt%Ce alloys display different corroded feature, and the potential difference between Al_4Ce and α-Al phases causes the galvanic corrosion.

3) The corrosion rate of Al-xCe alloys increases in following order: Al-15wt%Ce > Al-50wt%Ce > Al-30wt%Ce, which is attributed to different corrosion behaviors related to the volume fraction of Al_4Ce phases.

ACKNOWLEDGEMENT
This work was financially supported by the Project of Enterprise Sci-tech Commissioner (GDKTP2020013500).

References

1. H. Xiong, L. Su, C. Kong, H. Yu, Adv. Eng. Mater., 23 (2021) 2001533.
2. F. M. Mwema, O. P. Oladijo, S. A. Akinlabi, E.T.Akinlabi, *J. Alloys Compd*., 747 (2018) 306.
3. U. Barajas-Valdes, O. M. Suárez, *Thin Solid Films*, 693 (2020) 137670.
4. R. Xu, *J. Phys.: Conf. Ser*., 1670 (2020) 12029.
5. A. K. Saikumar, S. D. Nehate, K. B. Sundaram, *Crit. Rev. Solid State Mater. Sci*., (2021) 1.
6. H. Garbacz, P. Wieciński, B. Adamczyk-Cieślak, J. Mizera, K. J. Kurzydłowski, *J. Microsc*., 237 (2010) 475.
7. A. Baptista, F. Silva, J. Porteiro, J. Míguez, G. Pinto, *Coatings*, 8 (2018) 402.
8. J. Tao, J. Liu, L. Chen, H. Cao, X. Meng, Y. Zhang, C. Zhang, L. Sun, P. Yang, J. Chu, *Green Chem*., 18 (2016) 550.
9. T. Onishi, E. Iwamura, K. Takagi, K. Yoshikawa, *J. Vac. Sci. Technol.,* A, 14 (1996) 2728.
10. V. Balaram, *Geosci. Front*., 10 (2019) 1285.
11. K. Habib, H. Wenzel, *J. Cleaner Prod*., 84 (2014) 348.
12. Z. C. Sims, O. R. Rios, D. Weiss, P. E. A. Turchi, A. Perron, J. R. I. Lee, T. T. Li, J. A. Hammons, M. Bagge-Hansen, T. M. Willey, K. An, Y. Chen, A. H. King, S. K. McCall, *Mater. Horiz*., 4 (2017) 1070.
13. D. Weiss, Castability and characteristics of high cerium aluminum alloys, *Advanced Casting Technologies*, (2017).
14. M. A. Dominguez-Crespo, A. M. Torres-Huerta, S. E. Rodil, E. Ramírez-Meneses, G.G.Suárez-Velázquez, M. A. Hernández-Pérez, *Electrochim. Acta*, 55 (2009) 498.
15. A. Lisenkov, M. L. Zheludkevich, M. G. S Ferreira, *Electrochem. Commun*., 12 (2010) 729.
16. R. T. Nguyen, D. D. Imholte, O. R. Rios, D. Weiss, Z. Sims, E. Stromme, S. K. McCall, *Resour. Conserv. Recycl*., 144 (2019) 340.
17. B. R. Powell, V. Rezhets, M. P. Balogh, R. A. Waldo, *Jom*, 54 (2002) 34.
18. Z. Wang, P. Chen, H. Li, B. Fang, R. Song, Z. Zheng, *Corros. Sci*., 114 (2017) 156.
19. J. F. Li, C. X. Li, Z. W. Peng, W. J. Chen, Z. Q. Zheng, *J. Alloys Compd*., 460 (2008) 688.
20. C. Liu, Z. Ren, Y. Xu, S. Pang, X. Zhao, Y. Zhao, *Scanning*, 2018.
21. X. Zhang, Z. Wang, Z. Zhou, J. Xu, *J. Mater. Eng. Perform*., 25 (2016) 1122.
22. Z. H. Huang, X. F. Guo, Z. M. Zhang, C. J. Xu, *Acta Metall. Sin*., 18 (2005) 129.
23. J. G. Brunner, N. Birbilis, K. D. Ralston, S.Virtanen, *Corros. Sci*., 57 (2012) 209.
24. L. Feng, Q. Pan, L. Wei, Z. Huang, Z. Liu, *J. Cent. South Univ*., 22 (2015) 2423.
25. P. L. M. Kanta, V. C. Srivastava, K. Venkateswarlu, S. Paswan, B. Mahato, G. Das, K. Sivaprasad, K. Gopala Krishna, *Int. J. Miner. Metall. Mater*., 24 (2017) 1293.
26. J. Ma, J. Wen, G. Li, X.V. Chunhua, *Corros. Sci*., 52 (2010) 534.
27. X. Li, W. Xia, H. Yan, J. Chen, X. Li, *Corros. Eng. Sci. Techn*., 55 (2020) 381.
28. X. Zhang, Z. Wang, Z. Zhou, J. Xu, *J. Alloys Compd*., 698 (2017) 241.